

Article

Self-Assembly of Free-Standing LiMn₂O₄-Graphene Flexible Film for High-Performance Rechargeable Hybrid Aqueous Battery

Guanghui Yuan ^{1,*}, Ting Huang ¹, Ying Kou ¹, Zhen Ji ¹ and Yan Zhao ^{2,*}

¹ Department of Chemistry and Chemical Engineering, Research Centre of New Materials, Ankang University, Ankang 725000, China; tingyu2008jh@126.com (T.H.); streamlet2000@163.com (Y.K.); jizhen@aku.edu.cn (Z.J.)

² Synergy Innovation Institute of GDUT, Heyuan 517000, China

* Correspondence: chem_yuan@163.com (G.Y.); zhaoyan_sii@163.com (Y.Z.); Tel.: +86-136-8915-5865; Fax: +86-0915-326-1415

Received: 8 May 2018; Accepted: 13 June 2018; Published: 21 June 2018



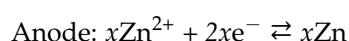
Abstract: A novel LiMn₂O₄-graphene flexible film is successfully prepared by facile vacuum filtration technique. LiMn₂O₄ nanowires with diameters of 50–100 nm are distributed homogeneously on graphene sheet matrix. Used as cathode in rechargeable hybrid aqueous batteries, the LiMn₂O₄-graphene film exhibits enhanced electrochemical performance in comparison to LiMn₂O₄-graphene powder. The LiMn₂O₄-graphene film shows stable 13.0 mAh g⁻¹ discharge capacity after 200 cycles at 1.0 C, benefitting from the presence of graphene with strong conductivity and large pore area in this free-standing film. This synthetic strategy for a free-standing film can provide a new avenue for other flexible materials and binder-free electrodes.

Keywords: LiMn₂O₄-graphene; flexible film; rechargeable hybrid aqueous batteries; electrochemical performance

1. Introduction

The new generation of the electronic equipment, such as light wearable electronic devices and electric vehicles with high energy density batteries, is accelerating the development of rechargeable batteries [1,2]. The traditional rechargeable lithium-ion batteries with organic electrolyte are facing fiercer and fiercer challenge due to their high cost and low safety [3,4]. Recently, aqueous rechargeable lithium batteries have attracted increasing attention in large-scale energy storage systems due to their lower toxicity, lower cost and better safety, thanks to water solutions instead of organic electrolytes [5]. Among these, the rechargeable hybrid aqueous battery (ReHAB) has been attracting increasing attention [6].

The ReHAB is composed of a zinc metal anode and a traditional cathode (such as LiFePO₄ and LiMn₂O₄), in which the Zn anode undergoes the reversible redox reaction, while the LiFePO₄ or LiMn₂O₄ cathode, for instance, undergoes lithium intercalation/de-intercalation. The electrochemical reactions can be written as follows.



Recent reports have presented Zn/LiCl + ZnCl₂/LiMn₂O₄, Zn/LiCH₃COO + Zn(CH₃COO)₂/LiFePO₄, and Zn/LiCH₃COO + Zn(CH₃COO)₂/MnO₂ ReHABs with different cathodes and electrolytes [7–9]. Limited by poor electronic conductivity, low lithium ion diffusion rate and drastic volume change,

the electrochemical properties of pristine LiFePO_4 or LiMn_2O_4 cathodes often deteriorate drastically with increasing of charge-discharge rates. To overcome these issues, one of the effective strategies is anchoring the active LiFePO_4 or LiMn_2O_4 particles into various porous carbon matrixes to enhance the electrical conductivity and suppress the volume change during cycling [10–12].

Among various carbon-based materials, graphene or reduced graphene oxide is always intensively investigated, due to the large specific surface area, extraordinary electronic transport property and high electrochemical stability. Some work has discussed the positive effect on the electrochemical properties of graphene-based LiFePO_4 or LiMn_2O_4 composites [12–14]. It is worth noting that most of this work is focused on powder graphene composites and their application in lithium rechargeable batteries with organic electrolyte. Recently, research into flexible films as binder-free electrodes for rechargeable batteries has developed rapidly to power new applications, such as light and soft wearable electronic devices [15,16]. Compared to carbon nanotubes and other carbon-based materials, it is most convenient to make graphene into flexible film because of its layered structure [17]. However, few works have discussed graphene-based flexible film electrodes for rechargeable hybrid aqueous batteries.

Herein, a free-standing LiMn_2O_4 -graphene flexible film is designed and prepared by a facile vacuum filtration method, and its electrochemical performance is investigated for the first time in ReHAB. Compared to the LiMn_2O_4 -graphene powder prepared by simple physical mixing and the slurry casting technique, the LiMn_2O_4 -graphene film exhibits an amazingly stable cycling ability and enhanced rate performance.

2. Materials and Methods

2.1. Materials Preparation

Graphene oxide (GO) was synthesized by natural flake graphite according to previous work [18]. LiMn_2O_4 powder was prepared by the following process. 0.095 g KMnO_4 was dissolved in 25 mL deionized (DI) water and underwent ultrasonic radiation for 0.5 h to form the first solution. The second solution was arranged by dissolving 0.220 $\text{Mn}(\text{CH}_3\text{COO})_2 \cdot 4\text{H}_2\text{O}$ in 25 mL DI water. The mixture of the two solutions was transferred and sealed in a 60 mL Teflon autoclave for 20 h at 160 °C. After the hydrothermal reaction, black MnO_2 powder was collected, followed by centrifugation, washing with ethanol and DI water, and drying in vacuum. The prepared MnO_2 and $\text{LiOH} \cdot \text{H}_2\text{O}$ powders with a molar ratio of 2:1 were ground with ethanol for 1 h. After air solid-state reaction at 400 °C for 8 h and 750 °C for 10 h, the expected LiMn_2O_4 powder (LMO) was prepared.

The flexible LiMn_2O_4 -graphene film was manufactured by an ordinary vacuum filtration method followed by a thermal reduction process. Typically, 30 mg GO was dispersed in 10 mL deionized water and underwent ultrasonic operation for 2 h to a uniform brown GO suspension. 20 mg LiMn_2O_4 powder was secondly dispersed into the GO suspension to undergo ultrasonic treatment for 2 h. The suspension was then filtered through a filter membrane under vacuum. The flexible film was peeled off carefully from the membrane after washing, drying and immersing in acetone for 15 min. After being heat treated in air at 220 °C for 2 h to reduce GO into graphene (GN), the final flexible LiMn_2O_4 -graphene film was obtained, labeled as LMO/GN-F. The preparation procedure and photos of the flexible film are shown in Figure 1. For comparison, the LiMn_2O_4 -graphene powder (LMO/GN-P) was prepared by simple physical ball-milling.

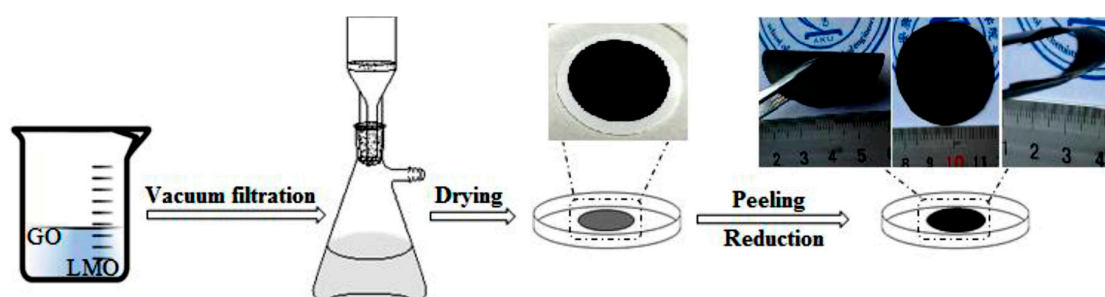


Figure 1. Schematic for the preparation process of the LiMn_2O_4 -graphene film.

2.2. Material Characterization

The crystalline phases of the as-prepared samples were determined by X-ray powder diffraction (XRD, D8 ADVANCE, Bruker, Billerica, MA, USA) equipped with $\text{Cu K}\alpha$ radiation ($\lambda = 0.15418 \text{ nm}$) at a scanning rate of $0.02^\circ \text{ s}^{-1}$ in $10\text{--}70^\circ$. The content of LiMn_2O_4 in the LiMn_2O_4 -graphene powder and the LiMn_2O_4 -graphene film were confirmed by thermoanalyzer (DSC-TGA; SDT Q600, TA Company, Boston, MA, USA) with air flow from room temperature to 600°C at $10^\circ \text{C min}^{-1}$. To determine the pore volumes and specific surface areas of the prepared films, Brunauer-Emmett-Teller (BET) and Barrette Joynere Halenda (BJH) methods were carried out using nitrogen adsorption. The surface morphologies of the samples were examined by field emission scanning electron microscopy (SEM, Quanta FEG-400) and transmission electron microscopy (TEM, FEI-Tecna G²-F20 S-TWIN) techniques.

2.3. Electrochemical Measurements

The free-standing LMO/GN-F electrodes were prepared by cutting the flexible LMO/GN film into 10 mm circles directly. The compared LMO/GN-P electrodes were prepared by brushing the *n*-methyl-2-pyrrolidinone slurry containing LMO/GN powder, acetylene black, and polyvinylidene fluoride (80:10:10 wt %) on 10 mm stainless steel foil, followed by vacuum drying at 110°C for one night. The stainless steel foil was pressed at 10 MPa to achieve superior contact between the active material and the current collector. The CR2025 coin cells were assembled using Zn metal as anode, 0.5 M LiCH_3COO and 0.5 M $\text{Zn}(\text{CH}_3\text{COO})_2$ aqueous solution as electrolyte, absorbent glass mat wet as separator, and the LMO/GN-F or LMO/GN-P electrode as cathode.

The cyclic voltammetry (CV) was carried out on a CHI 660D electrochemical workstation at a scan rate of 0.15 mV s^{-1} in the potential range of 1.35–2.15 V vs. Zn/Zn^{2+} . The galvanostatic charge-discharge tests were arranged on a LAND battery program-controlled tester in a cut-off potential window of 1.45–2.05 V. Electrochemical impedance spectroscopy (EIS) was performed by using the CHI 660D electrochemical workstation with a frequency range from 0.01 to 100 kHz.

3. Results and Discussion

Figure 2a shows the X-ray diffraction (XRD) patterns of the as-prepared samples. The XRD patterns of GO displays only one obvious peak centered at around 11.5° , which can be attributed to the (002) reflection of graphene oxide. The XRD patterns of GN display one obvious peak centered at around 25.6° and one weak peak at around 43.6° , which can be attributed to the (002) and (100) reflections of graphene, respectively [19]. The XRD pattern of LMO used in our experiment shows the typical reflection pattern of cubic spinel LiMn_2O_4 with a space group of $\text{Fd}\bar{3}\text{m}$ [20]. The XRD pattern of LMO/GN-F exhibits the characteristic features of spinel LiMn_2O_4 and a broad typical peak of graphene at around 25.6° , indicating that there are no phase transformations for LMO in the LMO/GN film. No detectable peak at around 11.5° is observed, indicating that graphene oxide is reduced completely to graphene during the experiment process. The XRD pattern of LMO/GN-P exhibits a very similar shape with the XRD pattern of LMO/GN-F, indicating that the LiMn_2O_4 -graphene composite can

be made successfully by the physical ball-milling technique. The LMO contents in the LMO/GN film and as-prepared LMO/GN powder are estimated by TGA under air atmosphere with a heating rate of $10\text{ }^{\circ}\text{C min}^{-1}$. Both LMO/GN-F and LMO/GN-P TGA curves in Figure 2b show only one drastic weight loss from around $300\text{ }^{\circ}\text{C}$ to $450\text{ }^{\circ}\text{C}$. From $450\text{ }^{\circ}\text{C}$ upon $600\text{ }^{\circ}\text{C}$, the two TGA curves remain approximately unchanged. The results indicate that the carbon component in LMO/GN-F and LMO/GN-P is completely burned in air flow [21,22]. The two TGA curves remain unchanged from $450\text{ }^{\circ}\text{C}$ to $600\text{ }^{\circ}\text{C}$, showing that the LMO in the two samples has no phase transformations during the heat treatment. The LMO/GN-F and LMO/GN-P exhibit around 44.2% and 48.5% LMO content, respectively. The similar amounts of LMO content in the different samples can eliminate the influence of different content on electrochemical performance.

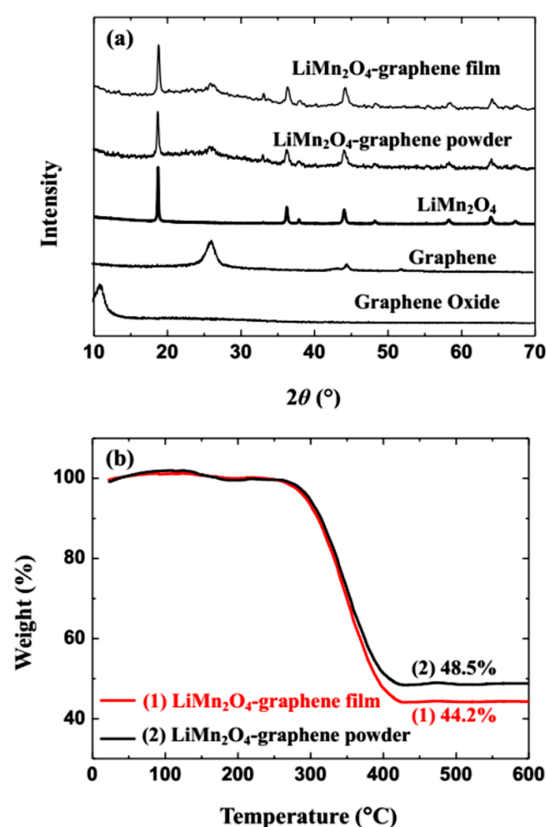


Figure 2. XRD patterns of samples (a), and thermogravimetric curves of LiMn₂O₄-graphene film and LiMn₂O₄-graphene powder (b).

The morphology of the synthesized LMO, GN film and LMO/GN film are measured by SEM (Figure 3). The LMO nanowires are 5–10 μm in length (Figure 3a). There is a slight agglomeration among LMO nanowires. The pristine GN film has curved and wrinkled surface morphology (Figure 3b). The LMO/GN film has a similar wrinkled surface to GN film, except that LMO nanowires are homogeneously distributed in the surface (Figure 3c). The thickness of the LMO/GN film is about 20 μm (Figure 3d). The fracture edge of this film displays layer-by-layer stacking of graphene sheets. To further determine the size of LMO nanowires and their distribution in the LMO/GN film, the samples are characterized by TEM. The pristine LMO nanowires have 50–100 nm in diameter (Figure 4a). The LMO nanowires are anchored uniformly in the LMO/GN film (Figure 4b) and exhibit the clear lattice fringes of LMO surrounded by unclear graphene polycrystalline lattice (Figure 4c). The selected area electron diffraction (SAED) pattern of the LMO (Figure 4d) is composed of spotted rings indexed to the (111), (311), (400), (222) and (331) planes of cubic LiMn₂O₄ inside and out. The SEM,

TEM images and the XRD patterns in Figure 2a clearly reveal that the LMO/GN film is prepared successfully by our facile vacuum filtration method.

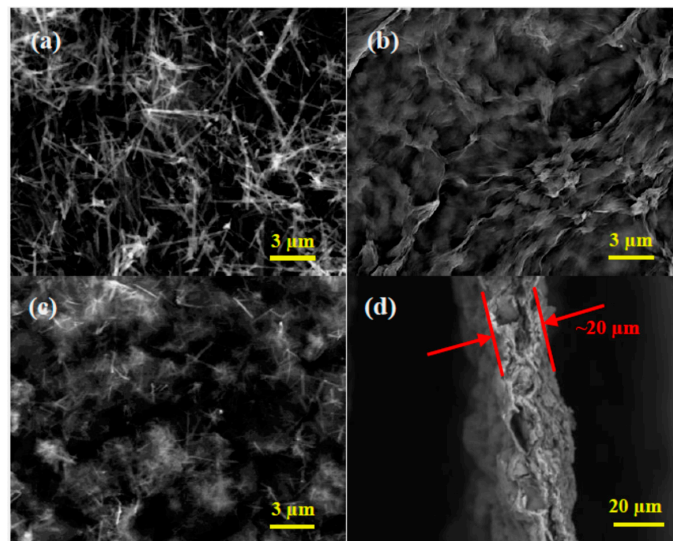


Figure 3. SEM images of LiMn_2O_4 (a), graphene film (b), surface (c), and fracture edge (d) of LiMn_2O_4 -graphene film.

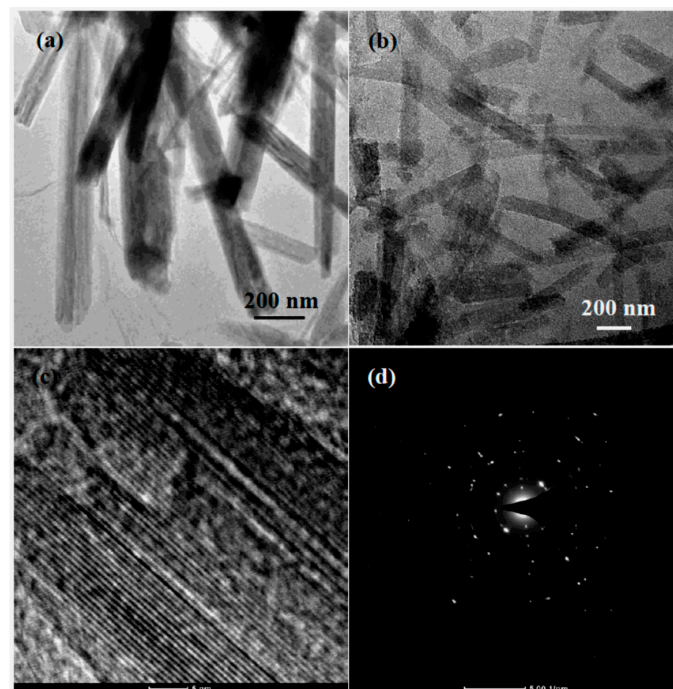


Figure 4. TEM images of LiMn_2O_4 (a), gradually enlarged TEM images (b,c), and SAED pattern (d) of the LiMn_2O_4 -graphene film.

In order to determine the specific surface area and pore volumes of the GN film and LMO/GN film, the N_2 adsorption and desorption isotherms are measured and shown in Figure 5. The BET specific surface area of the LMO/GN film is calculated to be $60.4 \text{ cm}^2 \text{ g}^{-1}$, which is obviously higher than that of the pristine GN film ($39.6 \text{ cm}^2 \text{ g}^{-1}$). This result can be attributed to the presence of LMO nanowires on or in the surface of the GN support. The LMO nanowires intercalating into the GN

nanosheets may not only result in more pores, but also prevent the aggregation of the GN nanosheets. In the meantime, the adsorption of the GN nanosheets can prevent the aggregation of the LMO nanowires. Therefore, the total pore volume of the LMO/GN film is $0.30 \text{ cm}^3 \text{ g}^{-1}$, which is higher than that of the pristine GN film ($0.21 \text{ cm}^3 \text{ g}^{-1}$). Combining the result with TEM measurements, the wrinkled surface morphology, large pore volume and specific surface area of the LMO/GN film can permit easy access for electrons and ions to the electrode/electrolyte and accommodate the volume change of the LMO nanowires during the charge and discharge process [23].

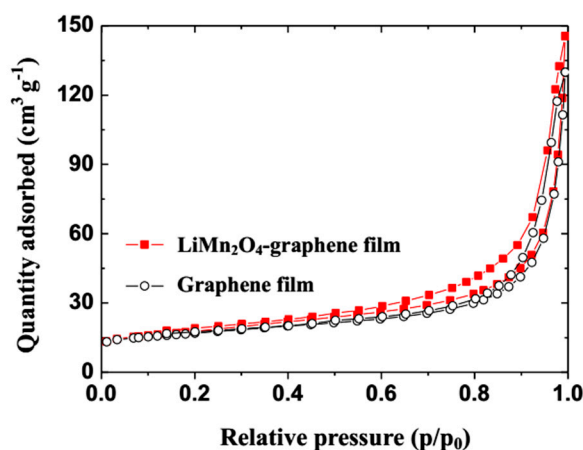


Figure 5. The N_2 isotherm adsorption and desorption curves of the graphene film and the LiMn_2O_4 -graphene film.

The galvanostatic discharge-charge and CV tests are important challenging and key aspects for ReHAB applications. Aiming to examine the electrochemical performance of the LMO/GN-F electrode sufficiently, the LMO/GN-F as cathode material for ReHAB is examined by CV and galvanostatic discharge-charge tests, as shown in Figure 6. All the CV curves over three cycles exhibit two obvious pairs of oxidation and reduction peaks between 1.6 and 2.0 V vs. Zn/Zn^{2+} , corresponding to the two-step lithium de/intercalation of the LMO/GN-F electrode (Figure 6a). In detail, the oxidation peak at 1.81 V is corresponding to the deintercalation of lithium ions from the spinel LiMn_2O_4 structure until half of the 8a sites are empty in $\text{Li}_x\text{Mn}_2\text{O}_4$ ($0.5 \leq x \leq 1$). The subsequent oxidation peak at 1.94 V corresponds to the continued deintercalation of lithium ions until all of the 8a sites are empty. At this point, LiMn_2O_4 is fully oxidized to $\lambda\text{-MnO}_2$. The anodic peak at 2.15 V vs. Zn/Zn^{2+} is assigned to O_2 evolution due to the water decomposition [6]. The reduction peak at 1.85 V is assigned to the intercalation of lithium ions into each available tetrahedral site (8a) in $\lambda\text{-MnO}_2$, until half of the sites are filled in $\text{Li}_x\text{Mn}_2\text{O}_4$ ($0 < x < 0.5$). The other reduction peak at 1.72 V is associated with the lithium ions filling the remaining empty 8a sites to form $\text{Li}_x\text{Mn}_2\text{O}_4$ ($0.5 \leq x \leq 1$) [24,25]. As clearly shown in the inset in Figure 6a, the peak intensity weakens slightly with increase in the CV test cycle, which could be due to the small attenuation of electrochemical activity. Figure 6b illustrates the first three charge-discharge profiles of the LMO/GN-F electrode at 0.5 C. According to the CV data, the potential of the charge-discharge process is restricted from 1.45 V to 2.05 V vs. Zn/Zn^{2+} to avoid the water decomposition. As shown in Figure 6b, all three curves have two well-defined plateaus at about 1.76 V and 1.92 V vs. Zn/Zn^{2+} in the charge and discharge profiles corresponding to the two-step lithium de/intercalation mechanism of LMO/GN-F electrode, which is confirmed by the CV data. The specific discharge capacities of LMO/GN-F electrode in the first three cycles are 121.1 (262.3–141.2), 120.4 (524.4–404.0) and 119.7 (786.0–666.3) mAh g^{-1} , respectively. The initial coulombic efficiency of LMO/GN-F electrode is around 85.7%. The low coulombic efficiency may be caused by the activation of the fresh electrode and the irreversible side reactions during the initial charge and discharge process.

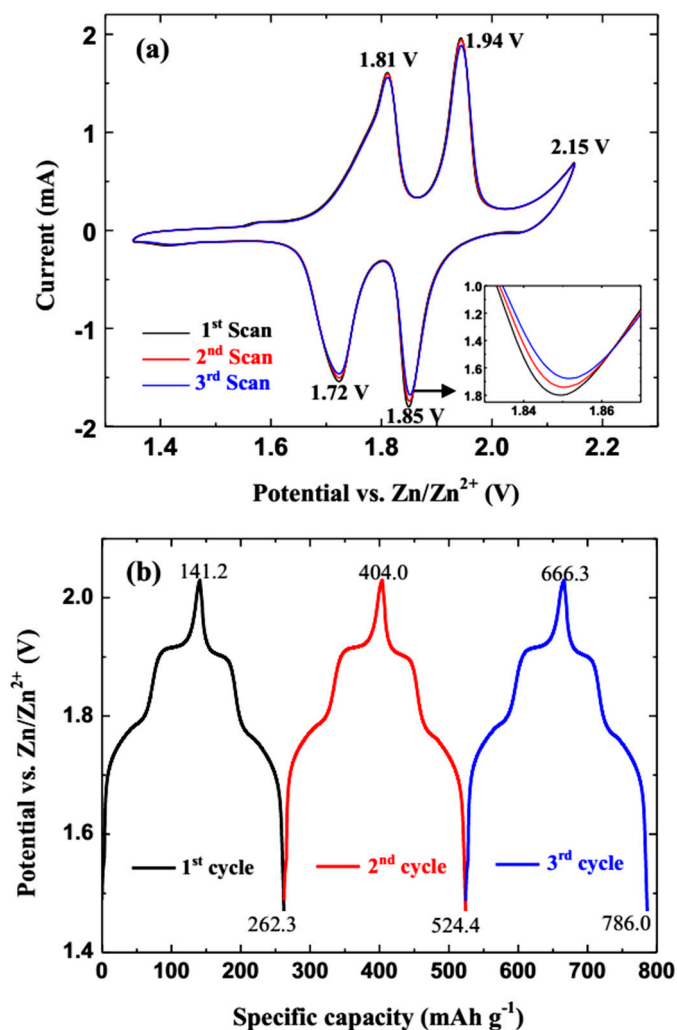


Figure 6. CV curves (a) and the initial charge-discharge profiles (b) of the LiMn_2O_4 -graphene film cathode at 0.2 C. Inset in (a) is the enlarged detail.

To further examine the effect of GN in improving the electrochemical performance sufficiently, the electrodes containing LMO/GN-P or LMO/GN-F as cathodes for ReHABs are tested for C-rate and cycle ability for comparison (Figure 7). As shown in Figure 7a, as the C-rate increases stepwise, the specific discharge capacities of both LMO/GN-P and LMO/GN-F electrodes decrease obviously, which is due to the diffusion-controlled kinetics of the lithium de/intercalation reactions [26]. Compared to LMO/GN-P, the rate performance of the LMO/GN-F is significantly improved (Figure 7a). In detail, for LMO/GN-F, the reversible discharge capacities of 122.5, 119.3, 112.1, 101.1 and 86.6 mAh g^{-1} are acquired at 0.5, 1.0, 2.0, 4.0 and 8.0 C, respectively. The returning of the C-rate back to 0.5 C can recover the discharge capacity of 120.6 mAh g^{-1} , indicating robustness of the LMO/GN flexible film. The long-term cyclabilities of the two electrodes are shown in Figure 7b. Both discharge capacities and capacity retentions of the LMO/GN-F electrode are obviously better than those of the LMO/GN-P electrode. After 200 cycles at 1.0 C, the discharge capacities of LMO/GN-F and LMO/GN-P electrodes are 113.0 mAh g^{-1} and 68.3 mAh g^{-1} . The corresponding capacity retentions are 94.8% and 76.7%, respectively. The coulombic efficiencies of both electrodes reached 99% after a few activated cycles. All the data indicate that the LiMn_2O_4 -graphene film exhibits an amazingly stable cycling ability and enhanced rate performance.

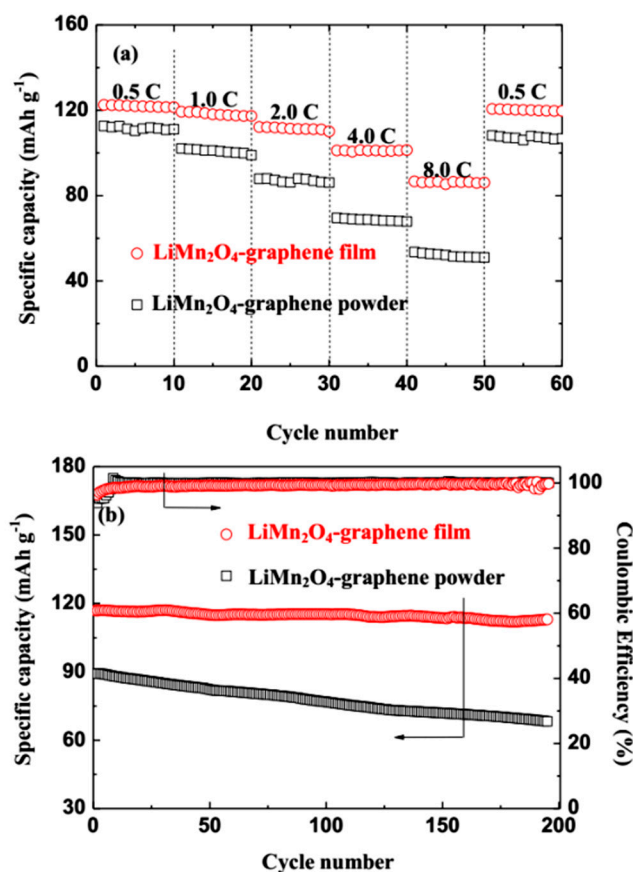


Figure 7. Rate capability (a) and cycle performance at 1C (b) of the LiMn₂O₄-graphene powder and LiMn₂O₄-graphene film cathodes.

Benefitting from the vacuum filtration method, the LMO nanowires and graphene sheets in LMO/GN-F contact each other more closely than in LMO/GN-P prepared by simple physical mixing. The improvement of electrochemical performance is mainly attributed to the positive effects of graphene in enhancing electronic conductivity [27], decreasing the LMO nanowires agglomeration and handling the volume expansion of LMO during charge-discharge cycles. The positive influence of the LMO/GN-F electrode on charge transfer behavior and conductivity of the system can be proved by the EIS measurements (Figure 8). As shown in Figure 8, both impedance plots of the LMO/GN-P and LMO/GN-F electrodes have the similar shape, which is composed of a semicircle in the high-to-medium frequency and a straight line in the low frequency. The slope angle of the straight line in the low-frequency region of the LMO/GN-F electrode is larger than that of the LMO/GN-P electrode, demonstrating that the LMO/GN-F electrode has a smaller Warburg impedance (W), resembling the solid-state diffusion of within the electrode [28,29]. The diameter of the semicircle in the high- to medium-frequency region for LMO/GN-F electrode is about 15 Ω , which is significantly smaller than that of the LMO/GN-P electrode (about 25 Ω), indicating that the LMO/GN-F electrode has a lower charge-transfer resistance (R_{ct}) at the electrode/electrolyte interface. The equivalent circuits are inset in Figure 8. In addition to W and R_{ct} , discussed above, R_{Ω} is the ohmic resistance representing the total resistance of the electrolyte, separator, and electrical contacts. CPE is the constant phase-angle element, involving double layer capacitance of the active materials. The enhancement of charge transfer and Li⁺ diffusion in combination with the lower aggregation of LiMn₂O₄ nanowires and the better volume change handling could lead to the superior electrochemical performance of the LMO/GN flexible film.

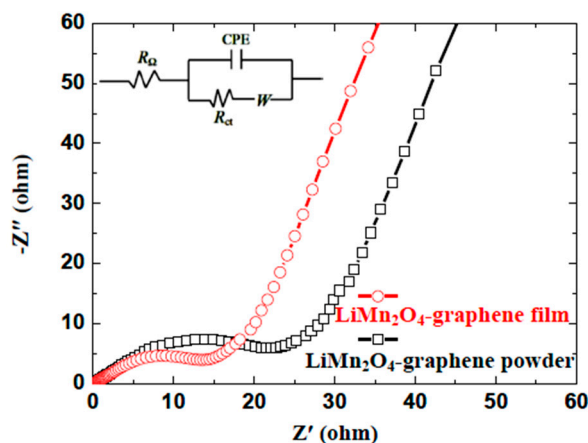


Figure 8. Nyquist plots of the LiMn_2O_4 -graphene film and LiMn_2O_4 -graphene powder cathodes after the first cycle showing the whole frequency region of 100 kHz to 0.01 Hz.

4. Conclusions

A flexible LMO/GN hybrid film was successfully prepared through a facile vacuum filtration and reduction process. Compared to the LMO/GN powder prepared by physical mixing, the designed LMO/GN film exhibits significantly enhanced electrochemical performance as cathodes in ReHABs. Benefited from the wrinkled surface and relatively large pore volume and specific surface area, the LMO/GN film could deliver reversible discharge capacities of 122.5, 119.3, 112.1, 101.1 and 86.6 mAh g^{-1} at 0.5, 1.0, 2.0, 4.0 and 8.0 C, respectively. Even after 200 charge-discharge cycles at 1.0 C, it could hold a high discharge capacity of 113.0 mAh g^{-1} . The improvement of the electrochemical performance for LMO/GN film in ReHABs is mainly a result of the enhanced electronic conductivity and convenient Li^+ transportation provided by graphene sheets, together with the positive effects of graphene in handling the aggregation and volume change of LMO nanowires.

Author Contributions: G.Y. designed the experiments. G.Y., H.T., Y.K. and Z.J. carried out the experiments and analyzed the data. G.Y., T.H. and Y.Z. contributed in the drafting and revision of the manuscript. Y.K. and G.Y. supervised the work and finalized the manuscript. All authors read and approved the final manuscript.

Funding: This research received no external funding.

Acknowledgments: The authors are grateful of financial support by the Natural Science Fund and Subject Merging Fund of Ankang University for high-level talents (Grant Nos. 2016AYQDZR05 and 2017AYJC01), the Natural Science Fund of Education Department of Shaanxi Provincial Government (Grant No. 15JK1004), and Natural Science Basic Research Plan in Shaanxi Province (Grant No. 2014JM2-2012).

Conflicts of Interest: The authors declare no conflict of interest.

References

- Lu, J.; Chen, Z.; Ma, Z.; Pan, F.; Curtiss, L.A.; Amine, K. The role of nanotechnology in the development of battery materials for electric vehicles. *Nat. Nanotechnol.* **2016**, *11*, 1031–1038. [[CrossRef](#)] [[PubMed](#)]
- Xia, X.H.; Chao, D.L.; Zhang, Y.Q.; Shen, Z.X.; Fan, H.J. Three-dimensional graphene and their integrated electrodes. *Nano Today* **2014**, *9*, 785. [[CrossRef](#)]
- Goriparti, S.; Miele, E.; De Angelis, F.; Di Fabrizio, E.; Zaccaria, R.P.; Capiglia, C. Review on recent progress of nanostructured anode materials for Li-ion batteries. *J. Power Sources* **2014**, *257*, 421–443. [[CrossRef](#)]
- Dell’Era, A.; Pasquali, M.; Bauer, E.M.; Vecchio Cipriotti, S.; Scaramuzzo, F.A.; Lupi, C. Synthesis, characterization, and electrochemical behavior of $\text{LiMn}_x\text{Fe}_{(1-x)}\text{PO}_4$ composites obtained from phenylphosphonate-based organic-inorganic hybrids. *Materials* **2017**, *11*, 56. [[CrossRef](#)] [[PubMed](#)]
- Wu, X.; Yuan, X.; Yu, J.; Liu, J.; Wang, F.; Fu, L.; Wu, Y. A high-capacity dual core-shell structured MWCNTs@S@PPy nanocomposite anode for advanced aqueous rechargeable lithium batteries. *Nanoscale* **2017**, *31*, 11004–11011. [[CrossRef](#)] [[PubMed](#)]

6. Yan, J.; Wang, J.; Liu, H.; Bakenov, Z.; Gosselink, D.; Chen, P. Rechargeable hybrid aqueous batteries. *J. Power Sour.* **2012**, *216*, 222–226. [[CrossRef](#)]
7. Yuan, G.; Bai, J.; Doan, T.N.L.; Chen, P. Synthesis and electrochemical investigation of nanosized LiMn_2O_4 as cathode material for rechargeable hybrid aqueous batteries. *Mater. Lett.* **2014**, *137*, 311–314. [[CrossRef](#)]
8. Zhao, S.; Han, B.; Zhang, D.; Huang, Q.; Xiao, L.; Chen, L.; Ivey, D.G.; Deng, Y.; Wei, W. Unravelling the reaction chemistry and degradation mechanism in aqueous Zn/ MnO_2 rechargeable batteries. *J. Mater. Chem. A* **2018**. [[CrossRef](#)]
9. Tang, W.; Hou, Y.; Wang, F.; Liu, L.; Wu, Y.; Zhu, K. LiMn_2O_4 nanotube as cathode material of second-level charge capability for aqueous rechargeable batteries. *Nano Lett.* **2013**, *13*, 2036–2040. [[CrossRef](#)] [[PubMed](#)]
10. Zhi, J.; Bertens, K.; Yazdi, A.Z.; Chen, P. Acrylonitrile copolymer/graphene skinned cathode for long cycle life rechargeable hybrid aqueous batteries at high-temperature. *Electrochim. Acta* **2018**, *268*, 248–255. [[CrossRef](#)]
11. Zhu, X.; Hoang, T.K.A.; Chen, P. Novel carbon materials in the cathode formulation for high rate rechargeable hybrid aqueous batteries. *Energies* **2017**, *10*, 1844. [[CrossRef](#)]
12. Yuan, G.; Bai, J.; Doan, T.N.L.; Chen, P. Synthesis and electrochemical properties of LiFePO_4 /graphene composite as a novel cathode material for rechargeable hybrid aqueous battery. *Mater. Lett.* **2015**, *158*, 248–251. [[CrossRef](#)]
13. Pyun, M.H.; Park, Y.J. Graphene/ LiMn_2O_4 nanocomposites for enhanced lithium ion batteries with high rate capability. *J. Alloy. Comp.* **2015**, *643*, S90–S94. [[CrossRef](#)]
14. Lin, B.; Yin, Q.; Hu, H.; Lu, F.; Xia, H. LiMn_2O_4 nanoparticles anchored on graphene nanosheets as high-performance cathode material for lithium-ion batteries. *J. Solid State Chem.* **2014**, *209*, 23–28. [[CrossRef](#)]
15. Chen, L.; Chen, L.; Ai, Q.; Li, D.; Si, P.; Feng, J.; Ci, L. Flexible all-solid-state supercapacitors based on freestanding, binder-free carbon nanofibers@polypyrrole@graphene film. *Chem. Eng. J.* **2018**, *334*, 184–190. [[CrossRef](#)]
16. Wang, B.; Ryu, J.; Choi, S.; Song, G.; Hong, D.; Hwang, C.; Chen, X.; Wang, B.; Li, W.; Song, H.K.; et al. Folding graphene film yields high areal energy storage in lithium-ion batteries. *ACS Nano* **2018**, *12*, 1739–1746. [[CrossRef](#)] [[PubMed](#)]
17. Lee, S.H.; Kang, D.; Oh, I.K. Multilayered graphene-carbon nanotube-iron oxide three-dimensional heterostructure for flexible electromagnetic interference shielding film. *Carbon* **2017**, *111*, 248–257. [[CrossRef](#)]
18. Zhao, J.; Pei, S.; Ren, W.; Gao, L.; Cheng, H.M. Efficient preparation of large-area graphene oxide sheets for transparent conductive films. *ACS Nano* **2010**, *4*, 5245–5252. [[CrossRef](#)] [[PubMed](#)]
19. Endo, M.; Takeuchi, K.; Hiroka, T.; Furuta, T.; Kasai, T.; Sun, X.; Kiang, C.H.; Dresselhaus, M.S. Stacking nature of graphene layers in carbon nanotubes and nanofibres. *J. Phys. Chem. Solids* **1997**, *58*, 1707–1713. [[CrossRef](#)]
20. Qu, Q.; Fu, L.; Zhan, X.; Samuelis, D.; Maier, J.; Li, L.; Tian, S.; Li, Z.; Wu, Y. Porous LiMn_2O_4 as cathode material with high power and excellent cycling for aqueous rechargeable lithium batteries. *Energy Environ. Sci.* **2011**, *4*, 3985–3990. [[CrossRef](#)]
21. Zhang, M.G.; Smith, A.; Gorski, W. Carbon nanotube-chitosan system for electrochemical sensing based on dehydrogenase enzymes. *Anal. Chem.* **2004**, *76*, 5045–5050. [[CrossRef](#)] [[PubMed](#)]
22. Wang, X.; Chen, K.; Wang, G.; Liu, X.; Wang, H. Rational design of three-dimensional graphene encapsulated with hollow FeP @carbon nanocomposite as outstanding anode material for lithium ion and sodium ion batteries. *ACS Nano* **2017**, *11*, 11602–11616. [[CrossRef](#)] [[PubMed](#)]
23. Wang, B.; Wang, G.; Lv, Z.; Wang, H. In situ synthesis of hierarchical CoFe_2O_4 nanoclusters/graphene aerogels and their high performance for lithium-ion batteries. *Phys. Chem. Chem. Phys.* **2015**, *17*, 27109–27117. [[CrossRef](#)] [[PubMed](#)]
24. Liu, W.; Kowal, K.; Farrington, G.C. Mechanism of the electrochemical insertion of lithium into LiMn_2O_4 spinels. *J. Electrochem. Soc.* **1998**, *145*, 459–465. [[CrossRef](#)]
25. Lu, D.; Li, W.; Zuo, X.; Yuan, Z.; Huang, Q. Study on electrode kinetics of Li^+ insertion in $\text{Li}_x\text{Mn}_2\text{O}_4$ ($0 \leq x \leq 1$) by electrochemical impedance spectroscopy. *J. Phys. Chem. C* **2007**, *111*, 12067–12074. [[CrossRef](#)]
26. Bakierska, M.; Świątosławski, M.; Dziembaj, R.; Molenda, M. Nature of the electrochemical properties of sulphur substituted LiMn_2O_4 spinel cathode material studied by electrochemical impedance spectroscopy. *Materials* **2016**, *9*, 696. [[CrossRef](#)] [[PubMed](#)]
27. Punczt, C.; Muckel, F.; Wolff, S.; Aksay, I.A.; Chavarin, C.A.; Bacher, G.; Mertin, W. The effect of degree of reduction on the electrical properties of functionalized graphene sheets. *App. Phys. Lett.* **2013**, *102*, 023114. [[CrossRef](#)]

28. Li, K.; Lin, S.; Shua, F.; Zhang, J.; Chen, K.; Xue, D. A rapid combustion route to synthesize high-performance nanocrystalline cathode materials for Li-ion batteries. *Cryst. Eng. Comm.* **2014**, *16*, 10969–10976. [[CrossRef](#)]
29. Aurbach, D. Electrode–solution interactions in Li-ion batteries: a short summary and new insights. *J. Power Sour.* **2003**, *119*, 497–503. [[CrossRef](#)]



© 2018 by the authors. Licensee MDPI, Basel, Switzerland. This article is an open access article distributed under the terms and conditions of the Creative Commons Attribution (CC BY) license (<http://creativecommons.org/licenses/by/4.0/>).